Retraction dynamics of water droplets after impacting upon solid surfaces from hydrophilic to superhydrophobic

Fujun Wang and Tiegang Fang ⓘ[*]
Department of Mechanical and Aerospace Engineering, North Carolina State University,
Raleigh, North Carolina 27695, USA

Although droplet retraction is involved in many applications, it receives less attention than droplet spreading. We present a detailed study of the retraction dynamics for water droplets with varying velocities impacting onto surfaces ranging from hydrophilic to superhydrophobic. The morphologies of retracting droplets are compared in detail. Two distinct retraction modes are classified: the inertial mode and the capillary mode. The retracting droplet with an inertial mode features a rim-lamella structure with a slowly decreasing dynamic receding contact angle while the capillary mode shows a collapsed rim and lamella and capillary wave propagation. During the retraction process, the inertial mode first takes place, and then the capillary mode occurs at a later stage. The inertial mode becomes more dominant with increasing impacting velocities. The dependencies of the retraction rate on impacting velocities and surface wettabilities are justified from the experimental measurements. The inertial-mode retraction rate increases with increasing velocity, while the capillary-mode retraction rate decreases. The retraction rate is generally higher for more hydrophobic surfaces, and its dependence on impacting velocities becomes stronger. An improved shape assumption for the retracting droplet is proposed by introducing an averaged dynamic receding contact angle and a shape factor. This semiempirical model can well explain the dependency of the inertial-mode retraction rate on impacting velocities for water droplets. Last but not the least, the normalized retraction curves generally collapse into a universal curve, revealing certain similarity behaviors for the droplet retraction on solid surfaces.

I. INTRODUCTION

Retraction of impacting droplets upon partially wettable surfaces is usually observed following the impact-induced spreading process. For hydrophobic/superhydrophobic substrates, part of or even the whole impacting droplet can rebound off the surface. Efforts have been devoted over the last 20 years to either enhancing [1–10] or inhibiting [11–19] the retraction process, depending on the applications. For applications such as inkjet printing, pesticide deposition on crops [17,20], thermal-/electro-spray coating [21,22], and spray cooling, an efficient deposition of droplets and longer contact time on the solid surfaces are desired. On the other hand, for the fabrication of substrates with the ability of self-cleaning [23] and anti-icing [24], a strong retraction process and a reduced contact time should be achieved.

Motivated by controlling the retraction process, the potential influencing factors on droplet retraction have been extensively studied. Dilute particles laden in an aqueous phase, such as nanoparticles [14], polymers [11,14] and surfactants [13,19], have been shown to significantly alter

---

[*]Corresponding author: tfang2@ncsu.edu

the droplet retraction process and thus suppress droplet rebound. However, the mechanism of how these polymer particles affect the retraction process is still in debate [11,25]. Other important factors include the surface temperature [26–28], surface micro- and macrostructure [3,6,10,29], surface motion [18,30], surface elasticity/viscoelasticity/flexibility [7,15,31,32], ambient pressure [4], and asymmetry of the impacting droplet [16,33,34].

All the investigations above mostly focused on two important parameters that characterize the droplet retraction process, namely, the contact time and the retraction speed $V_{\mathrm{ret}} = \max[-\dot{R}(t)]$, or retraction rate $\dot{\epsilon} = V_{\mathrm{ret}}/R_m$. $R(t)$ is the temporal evolution of the droplet spreading radius, and R_m denotes the maximum spread radius achieved at the end of spreading process. The contact time of a bouncing drop on a superhydrophobic surface was first investigated by Richard $et\ al.$ [35] with a conclusion that the contact time does not depend on the impact velocities within the investigated range $(0.2 - 2.3\,\mathrm{m/s})$. Later, it was further shown by Okumura $et\ al.$ [36] that the contact time significantly increases at a low impact velocity $(<0.1\,\mathrm{m/s})$. The plateau contact time at a large impact velocity is found to be well scaled as $\sim(\rho R_0^3/\sigma)^{1/2}$, which is the same as the period of free drop vibration derived by Rayleigh [37]. More recently, Antonini $et\ al.$ [38] identified an intermediate phase between the moment when the impacting droplet stops spreading and when it starts to recoil, which is characterized by the time elapsed at the maximum spreading, Δt_β. It is found that Δt_β is in the order of a few milliseconds. Moreover, Δt_β is found to decrease with increasing Weber number (We $= \rho D_0 V_0^2/\sigma$) and decreasing surface wettability.

The pioneering research in the retraction rate was conducted by Bartolo $et\ al.$ [39]. Aqueous droplets with different viscosities were used for droplet impacting experiments on a hydrophobic surface with relatively high impact velocities. It was first shown that the normalized retraction curves ($[R(t)/R_m]$ vs [t]) collapse into a single curve, and the corresponding retraction rate does not depend on the impact velocity. Moreover, they demonstrated a dynamic transition from an inertia receding regime to a viscous receding regime with an increasing Ohnesorge number (Oh $= \mu/\sqrt{\rho\sigma D_0}$). A semiquantitative model for the retraction rate was derived from the classical theories for thin film dewetting [40,41]. This model was later validated by Eggers $et\ al.$ [42] when theoretically studying the motion of the surrounding rim and the central lamella. The theory was further modified by Zhu $et\ al.$ [43] when numerically investigating the droplet retraction on a solid sphere, and Damak and Varanasi [44] when studying the retraction dynamics for drop-on-drop impacts on nonwetting surfaces. However, a recent experimental work by Bobinski $et\ al.$ [45] showed that the droplet retraction rate does depend on the impact velocity. They also demonstrated that for a smaller droplet diameter the dependency of the retraction rate on the impact velocity is stronger.

The brief review shows the importance of droplet retractions in many applications. However, the retraction dynamics of impacting droplets onto solid surfaces and its influencing factors are still not well understood. Compared to the amount of research in modeling the maximum spread factor, which is an important parameter characterizing the spreading process for an impacting droplet, the fundamental study of the retraction rate characterizing the receding process has received much less attention. The study of retraction dynamics by Bartolo $et\ al.$ [39] was limited to one substrate with a specific static receding contact angle, $\theta_{r,s} = 85°$. Although there have been some succeeding works [21,26,38,46] discussing the retraction of water droplets on surfaces with a wide range of wettability, the retraction dynamics was not investigated in a comprehensive manner.

Moreover, it was found that the retraction curves on a Teflon substrate ($\theta_{r,s} = 85°$) shown in Fig. 1 cannot simply collapse into a universal shape as suggested by Bartolo $et\ al.$ [39]. The intermediate phase, noted by Antonini $et\ al.$ [38], has not received equal attention when studying the droplet retraction dynamics. To address these concerns, we have conducted droplet impacting experiments on a series of surfaces from hydrophilic to superhydrophobic with We ranging from as low as 0.1 to the order of 1000, in order to systematically investigate the droplet retraction dynamics. The parameter value of the current study falls within the inertia-capillary (IC) regime [39] as shown in Table I. In particular, the droplet retracting morphologies, distinct retraction modes and corresponding retraction rate, and the scaling of retraction curves are discussed. We hope that this
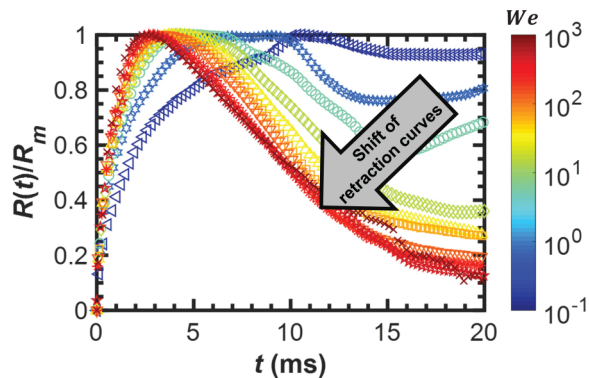
FIG. 1. Temporal evolution of the spreading factor $[R(t)/R_m]$ for water droplets impacting on a Teflon surface at We $= 0.1-1000$.

systematic analysis could provide fundamental knowledge for future study of retraction dynamics with more complexed liquids and surfaces.

II. METHODS AND MATERIALS

Six substrates with different wettabilities are used in the current study. Four of them are the same as used by Wang *et al.* [47]: microscope glass slide, acrylic sheet, silicon wafer, and Teflon sheet. Two superhydrophobic surfaces are added in this work. The first one is fabricated by sanding Teflon with a 220-grit sandpaper, as is proposed by Nilsson *et al.* [48]. The original, smooth Teflon plate has a thickness of 3 mm and it is mounted on a piece of glass to obtain a flat surface. Sanding has no preferred direction, and it takes approximately 1 minute. Then the sanded Teflon is cleaned with ethanol, rinsed with deionized water, and finally dried with compressed air.

The second superhydrophobic surface used here has been investigated and well characterized in some previous works [32,49]. It is fabricated by spraying a commercial superhydrophobic solution NeverWet onto a piece of clean glass. The two-layer coating process first sprays the base coat (without nanoparticles) onto the clean glass and then covers it with the top coating (with hydrophobic nanoparticles, $d_P \approx 50$ nm). In total, three layers of base coat and four layers of top coating are applied to make one superhydrophobic surface. The 2D- and 3D-reconstructed structures of the sanded Teflon and NeverWet-coated glass are illustrated in Figs. 2(a) and 2(b), respectively. The wettabilities of the six surfaces, including the quasistatic advancing ($\theta_{a,s}$) and receding ($\theta_{r,s}$) contact angles, are characterized by a sessile drop method using the same setup as Wang *et al.* [47]. The roughness of these surfaces is measured using a stylus profilometer (Mitutoyo Sj-310). Both the wettabilities and roughness are summarized in Table I, with STeflon standing for the sanded Teflon and Sglass for the superhydrophobic coated glass.

TABLE I. Wettabilities, roughness, and impact conditions for the six surfaces in current study

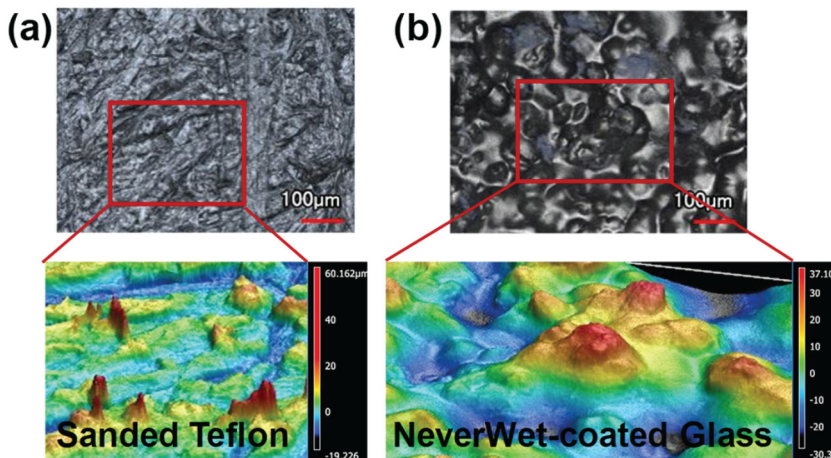| Substrates	Wettability	θ_a (deg)	θ_r (deg)	Ra (μm)	We	Oh
Glass	Hydrophilic	46 ± 2	21 ± 2	0.004 ± 0.001	$0.2 - 862$	
Acrylic	Hydrophilic	71 ± 3	49 ± 1	0.006 ± 0.001	$0.2 - 889$	
Silicon	Hydrophobic	92 ± 2	74 ± 2	0.004 ± 0.001	$0.1 - 737$	0.002
Teflon	Hydrophobic	107 ± 2	85 ± 2	0.35 ± 0.08	$0.2 - 912$	
STeflon	Superhydrophobic	146 ± 2	137 ± 3	3.41 ± 0.12	$0.8 - 847$	
Sglass	Superhydrophobic	158 ± 2	153 ± 1	4.87 ± 0.61	$0.6 - 829$	

FIG. 2. 2D and 3D images by confocal microscopy for (a) sanded Teflon and (b) NeverWet-coated glass.

As found by Antonini *et al.* [50], $\theta_{r,s}$ is a key wetting parameter affecting the droplet retraction. The broad range of $\theta_{r,s}$ ($21°-150°$) achieved in the current study is expected to show a relatively complete picture of how wettability influences the droplet retraction dynamics. The two hydrophilic surfaces (glass and acrylic) and the two hydrophobic surfaces (silicon and Teflon) are considered as smooth substrates. However, for the two superhydrophobic surfaces, transition from a Cassie-Baxter [51] to Wenzel [52] wetting state, which are considered for rough surfaces, can occur during droplet retraction.

The droplet retraction dynamics is recorded using a high-speed imaging system with more details described by Wang and Fang [53]. Specially, the imaging resolution is around $22\,\mu$m/pixel for We < 100 and $42\,\mu$m/pixel for We > 100, which enables us to capture a full impacting droplet at 4400 frames per second. The high-speed videos are subsequently processed via a customized image processing code in MATLAB. In the current study, a higher frame rate (45 454 fps) is also employed at a reduced resolution for selected We. Comparison between the 45 454-fps data and the 4400-fps data shows that the latter is capable of fully resolving the relatively slow droplet retraction process. Deionized (DI) water droplets are generated by a syringe pump equipped with a 24 gauge stainless-steel needle. The properties of DI water are as follows: density, $\rho = 998\,\text{kg/m}^3$; viscosity, $\mu = 8.9 \times 10^{-4}\,\text{Pa s}$; and surface tension, $\sigma = 71.97\,\text{dyn/cm}$. The generated droplet has a diameter of 2.5 ± 0.1 mm, and it impacts onto target surfaces from 10 different heights varying between 3 and 1600 mm. As a result, the impact velocity varies between 0.06 and 4.7 m/s.

III. MORPHOLOGY OF RETRACTING DROPLETS

Abundant phenomena during droplet retraction are observed from the high-speed videos, such as singular jets, partial rebound, total rebound, and receding breakup. Since most of these phenomena have been already reported in quite a few works, we would like to briefly summarize the observed phenomena with a focus on the droplet retraction process. All the image sequences below start from the maximum spread of the impacting droplet and end at the moment when the droplet finishes its retraction on the surface.

A. Hydrophilic and hydrophobic surfaces

Figures 3(a) and 3(b) demonstrate the droplet retraction process at selected times for different We on acrylic and Teflon. The scale is indicated by the red line segment. At a very low We ($\sim$1), the three-phase contact line (TPCL) remains pinned on acrylic, while on Teflon a slight retraction
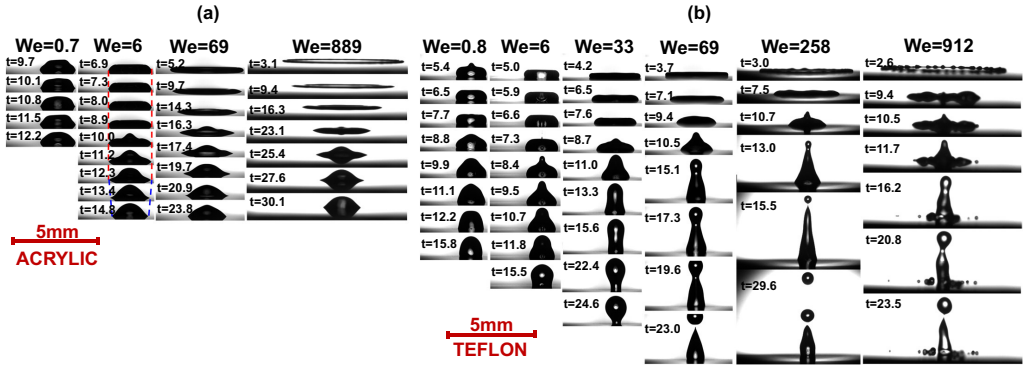
FIG. 3. Image sequences showing droplet retraction on (a) acrylic surface and (b) Teflon surface for selected We (units in ms).

can be detected. At a small We (∼6), droplet retraction can be temporally and spatially resolved on both surfaces. Initially, the top of the droplet silhouette remains flat and the contact angle stays almost the same, while its height is decreasing. This period is similar to the so-called "rim period" as observed by Wang and Fang [53], during which only the surrounding rim can be observed from the side-view images. Droplet retraction can start only when the central lamella is well beyond the height of the surrounding rim. For this type of droplet retraction, the contact angle is found to first decrease and then increase back at the end of the retraction process. One interesting thing noted here is the capillary wave propagation during the retraction process. The upper motion of the central lamella releases a capillary wave which propagates towards the TPCL along the droplet interface.

When We grows even higher, droplet retraction appears more obvious. Similarly, the contact angle has to decrease to a certain threshold before the TPCL can retract. The droplet first starts to retract on the surface while the contact angle does not experience much change. At a later stage of the retraction process, the central lamella grows higher and keeps moving upward. Like what is observed for the low-We case, the capillary wave brought by the upward motion of the central lamella gradually propagates toward the TPCL. The dynamic receding contact angle reaches its minimum when the capillary wave arrives at the TPCL. It should be noted here that the retraction discussed in this study refers only to the retraction of the TPCL of the major droplet on the surface. The tiny droplets generated for high We can hinder the view of the TPCL of the major droplet and make the algorithm detection inaccurate. In this case, manual detection was employed to find the correct TPCL position, which is the same case for the following superhydrophobic surfaces.

B. Superhydrophobic surfaces

Phenomena of drop impact on superhydrophobic surfaces have been well documented in Refs. [54,55]. Generally speaking, as shown in Fig. 4(a), superhydrophobicity is maintained on Sglass for all the investigated We. The retraction motion, for both the main and the satellite droplets, is so strong that all of them can totally bounce off the surface in the end. However, for STeflon, impalement transitions [56] occur starting from We ∼ 14 [see Fig. 4(b)], indicating a wetting state changing from the Cassie-Baxter type to the Wenzel type. The apparent TPCL is then always attached to the surface.

For very high We (∼862) on Sglass, the impacting droplet violently splashes into numerous tiny droplets during the spreading stage. No obvious apparent TPCL exists for the mother droplet. Instead, almost all the droplets are observed to simultaneously rebound off the surface, and, finally, a clean surface is left behind. Likewise, on STeflon, the mother droplet splashes into many satellite droplets. But those tiny droplets get pinned on the surface and are not able to rebound.
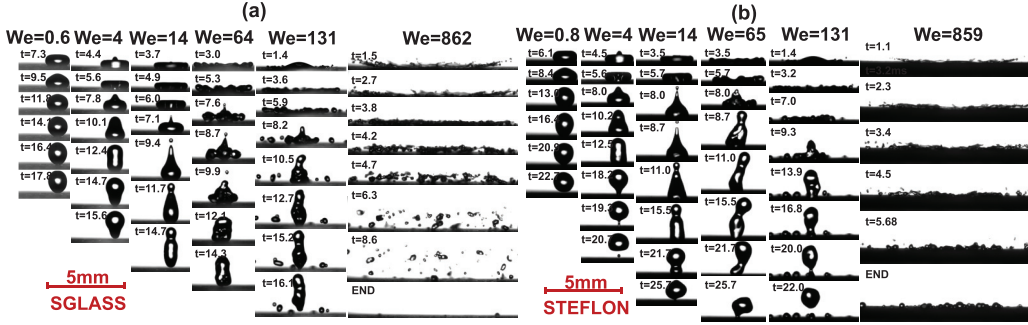
FIG. 4. Image sequences showing water droplet retraction on (a) Sglass and (b) STeflon for selected We (units in ms).

IV. DISCUSSION OF RETRACTION MODES

It has been revealed by Bartolo *et al.* [39] that for liquids with varying viscosities, there exist two retraction regimes: inertial and viscous. In the inertial regime, the retracting droplet features a surrounding rim and a central thin film. However, during the retraction process, a high-viscosity liquid droplet will quickly relax to a spherical shape, and the contact angle varies slowly. In this paper, we will show next that different retraction modes can also be temporally resolved during different stages of the retraction process for the low-viscosity liquid droplets.

A. Classification of three types of retraction modes

In the above discussion regarding the droplet retraction phenomena, the transition of the two typical retraction modes can be observed. The key difference between these two modes is the existence of a separate surrounding rim. Figure 5 presents the dynamic features of these two modes by overlapping the time-sequenced images. In the early stage of the retraction process, the internal interface of the surrounding rim is well separated, and this mode is named an inertial mode. For this mode, the dynamic receding contact angle and the rim height of the retracting droplet do not change significantly during the retraction process. This mode is the same as what is described as the inertial regime by Bartolo *et al.* [39]. Most of the theoretical work [42,43] on the droplet spreading and retraction with a high impacting velocity refers to this mode. In a later stage of the retraction process, the rim-lamella structure may not hold anymore. Instead, the internal interfaces of the surrounding rim collide with each other and generate upward momentum. Meanwhile, capillary waves are released from the top due to the collision of internal rims. The mobile-contact-line (MCL-mode)
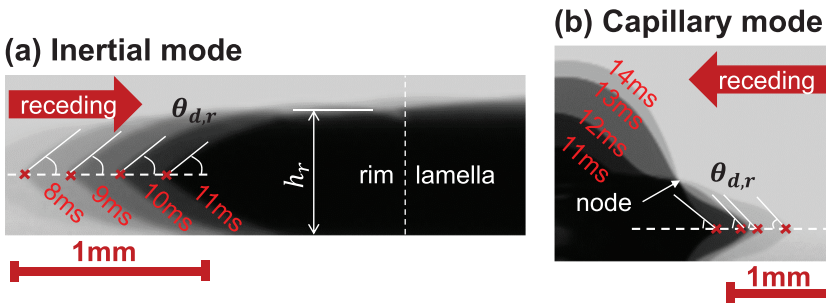

FIG. 5. Two modes of retraction for low-viscosity droplet retracting on silicon: (a) inertial mode during early stage at We = 113 and (b) capillary mode during later stage of the retraction process at We = 55.
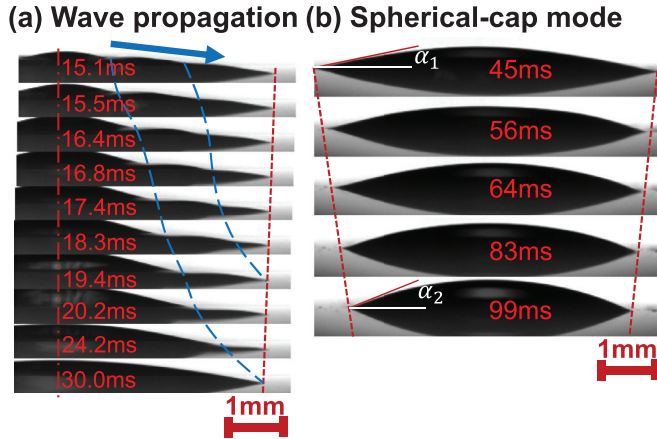
FIG. 6. (a) Capillary wave propagation along the interface of a retracting droplet on glass; (b) a distinct retraction mode exhibited by droplet retracting on glass at large times.

oscillation [53] of the droplet interface is clearly visible from the overlapped sequences. One node on the droplet interface can be observed from Fig. 5(b), which is consistent with the previous study [53] for MCL-type droplet oscillation on a solid surface. In this paper, we would like to name the second type of retraction the "capillary mode." In the capillary mode, the capillary force becomes comparable to the residual inertia force. The droplet interface keeps oscillating due to the propagation of the capillary wave from the top. The capillary oscillation can induce considerable TPCL retractions as shown in the morphologies (Figs. 3 and 4). For the capillary mode, the dynamic receding contact angle at the TPCL can become very low due to the capillary oscillation, which is believed to influence the retraction rate. It is worth noting that for low We, the maximum spreading diameter is not large enough for the rim to relax itself to the required receding contact angles. Therefore, the internal interfaces of the surrounding rim can easily collapse into each other even before the TPCL starts to retract. As a result, only the capillary mode is available for low-We droplet retraction.

In particular, there is a third mode demonstrated by the droplet retracting on glass, which has a very low $\theta_{r,s}$. During the capillary-mode retraction, the capillary wave propagates towards the TPCL as shown in Fig. 6(a). After a certain time, the capillary wave is fully damped, and the droplet then adopts a spherical-cap shape. Moreover, the droplet has not ceased its retraction yet. While maintaining its spherical-cap shape, the droplet keeps retracting with a very low speed for a long time. In such a spherical-cap mode, $\theta_{r,d}$ is observed to increase with time. It should be noted that the spherical-cap mode and the inertial mode were also characterized in a similar manner by Edwards *et al.* [57] when studying the retraction of a thin film into a sessile droplet.

B. Characterization of the inertial and capillary modes

In the above discussion, we have classified different retraction modes based on their morphologies. The question is: How can these distinct modes be characterized? Figure 7 shows a typical temporal evolution of the normalized spreading factor $[R(t)/R_m]$ and the dynamic receding contact angle ($\theta_{r,d}$) during the spreading-retraction process for a water droplet impacting on silicon. A slight decrease in the dynamic contact angle can be observed in Fig. 7. A decrease in the dynamic contact angle during the early stage of the retraction process was also found by de Goede *et al.* [58]. The insets in Fig. 7 denote the side view and tilted view of the retracting droplet. The transition from the inertial mode to the capillary mode can be clearly observed in Fig. 7, which features the appearance of an obvious oscillation of $\theta_{r,d}$ resulting from the propagation of the capillary waves.
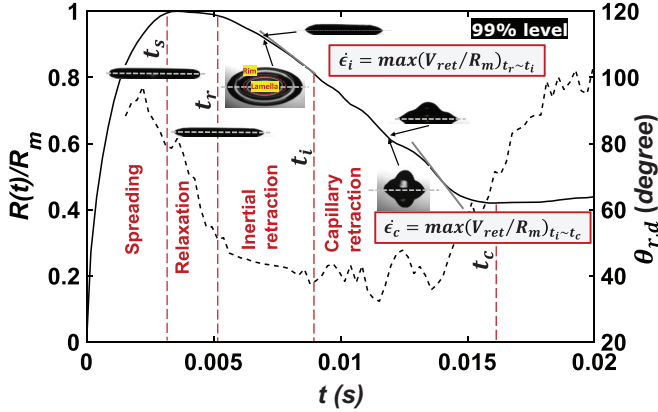
FIG. 7. Temporal evolution of the spreading diameter (solid line), 3D structure, and the dynamic contact angle (dashed line) of the retracting droplet.

Several key characteristic times need to be defined before we proceed to compare the two retraction modes. In Fig. 7 t_s and t_r represent the end of the spreading time and the start of the retraction time, respectively. We here use the same criterion (0.99 threshold) for the definition of t_s and t_r as used by Antonini *et al.* [38]: t_i and t_c denote the end of the inertial-mode retraction time and the capillary-mode retraction time, respectively. Clearly, the whole retraction process begins with the relaxation phase, followed by the inertial-mode retraction, and ends with the capillary-mode retraction. The periods of the inertial mode and the capillary mode can then be calculated as $T_i = t_i - t_r$ and $T_c = t_c - t_i$.

Figure 8 demonstrates the comparison between the normalized periods $[T_i/(T_i + T_c)$ and $T_c/(T_i + T_c)]$ of these two retraction modes. It clearly shows that the capillary mode occupies most of the retraction process for low-We conditions. With a higher We, the inertial mode starts to dominate the retraction process for surfaces with low $\theta_{r,s}$. However, for the surfaces with high $\theta_{r,s}$, although the inertial mode increases its proportion with increasing We, the capillary mode always dominates the retraction process.
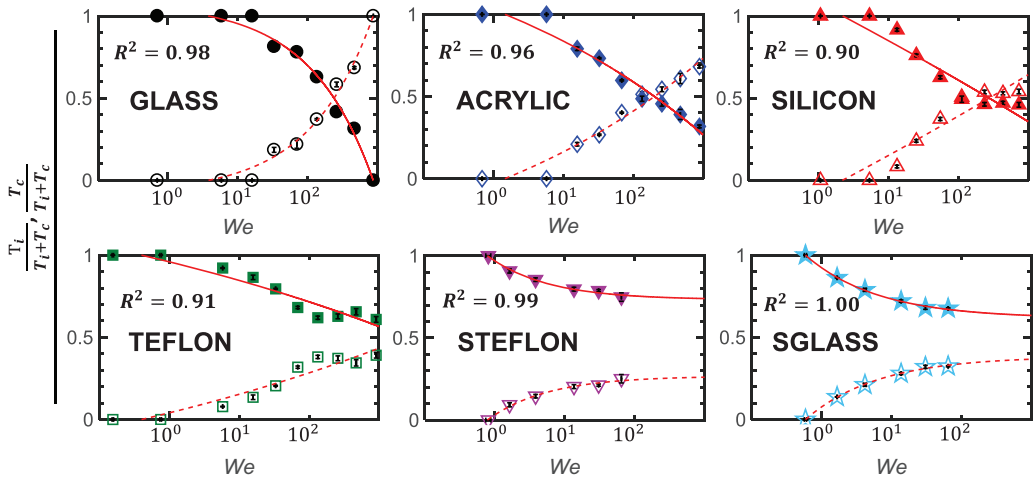

FIG. 8. Comparison of the periods occupied by the two retraction modes (dashed for inertial mode and solid for capillary mode).
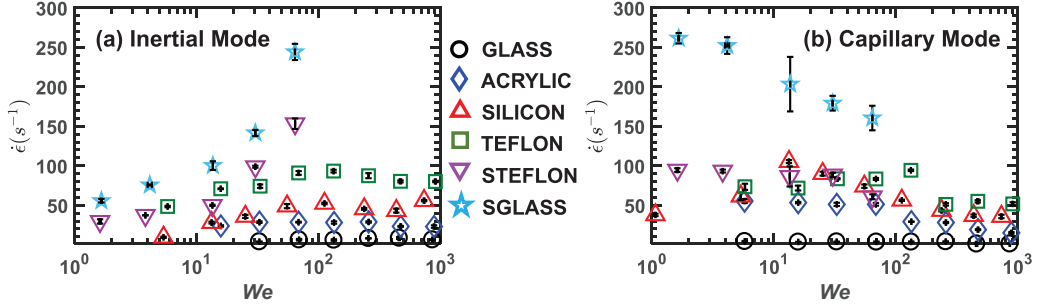
FIG. 9. The measurement of retraction rate for (a) inertial mode and (b) capillary mode.

C. Retraction rate for different modes

The classification of these distinct modes is important when calculating the droplet retraction rate ($\dot{\epsilon}$) and developing the corresponding theory for its prediction. The commonly used definition of $\dot{\epsilon}$ comes originally from Bartolo *et al.* [39]: $\dot{\epsilon} = \max(V_{\mathrm{ret}}/R_m)$. As the dynamics of the retracting droplets is different for different modes, it is necessary to calculate $\dot{\epsilon}$ for those distinct modes separately. The spherical-cap mode will not be considered in the comparison. After the determination of the occupied periods, we can safely define the corresponding retraction rate for the inertial and capillary modes as follows:

$$\dot{\epsilon}_i = \max\left(V_{\mathrm{ret}}/R_m\right)_{t_i \sim t_r}, \tag{1}$$

$$\dot{\epsilon}_c = \max\left(V_{\mathrm{ret}}/R_m\right)_{t_c \sim t_i}. \tag{2}$$

The measurement of $\dot{\epsilon}_i$ and $\dot{\epsilon}_c$ is demonstrated in Figs. 9(a) and 9(b) with error bars. The data are relatively repeatable. The relatively large deviation for Sglass is believed to come from the manual detection of the contact line as mentioned earlier. For Sglass and STeflon, only the data for We < 100 are included. As discussed in the above, receding breakup occurs on these two surfaces when We > 100. For nonsuperhydrophobic surfaces, the inertial mode does not exist for certain low-We cases. Therefore, some data points are missing in Fig. 9(a). For glass with We < 5, even the capillary-mode retraction vanishes.

The experimental results in Figs. 9(a) and 9(b) show the dependence of $\dot{\epsilon}$ on both the surface wettability and the impact condition. A comparison of the two modes indicates two different trends: $\dot{\epsilon}_i$ generally increases with increasing We, while $\dot{\epsilon}_c$ decreases with increasing We. At a small We, the expansion of the droplet during the spreading phase is not significant compared to its final equilibrium position. Therefore, this also makes the retraction rate smaller compared to the high-We conditions. More specifically, for the inertial mode, $\dot{\epsilon}_i$ continuously increases until around We = 60 for all the examined surfaces. When We > 60, $\dot{\epsilon}_i$ generally remains an asymptotic value and becomes wettability-dependent only. This indicates that the retraction rate for high We can be regarded as a material constant of the liquid-surface system, which is similar to what was observed by Bartolo *et al.* [39]. For low We on Sglass and STeflon, the increase of $\dot{\epsilon}_i$ from We < 10 to We > 60 is found to be significant, which is larger than 100%, as shown in Fig. 9(a). A similar increasing trend of the retraction rate was also noticed by Bobinski *et al.* [45] recently for superhydrophobic surfaces at small We. Several reasons are believed to be responsible for the ignorance of the increasing trend in the previous study [39]. First, the examined We started from a medium value (∼40), at which the asymptotic had almost been reached. Second, the inertial mode and the capillary mode were not differentiated when calculating the retraction rate. From Figs. 9(a) and 9(b), it is shown that at low We, $\dot{\epsilon}_c$ can be higher than $\dot{\epsilon}_i$. Therefore, the increasing trend of $\dot{\epsilon}_i$ will be compromised when the definition of $\dot{\epsilon}$ by Bartolo *et al.* [39] is used.
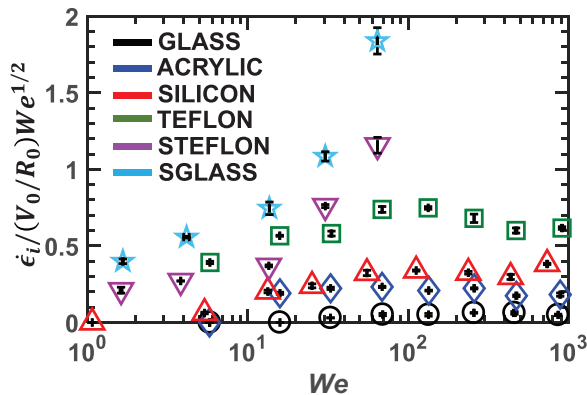
FIG. 10. Experimental data of the left-hand side term in Eq. (2) at different We for the six surfaces.

The effects of the surface wettability are clearly shown in Figs. 9(a) and 9(b). It acts in a reverse manner compared to the dynamic wetting effects in the spreading process [59]. For surfaces with higher $\theta_{r,s}$, the droplet retraction rate is higher, which is consistent with the classical retraction theory [39]. Moreover, it shows a stronger dependence on We for both $\dot{\epsilon}_i$ and $\dot{\epsilon}_c$ on surfaces with higher $\theta_{r,s}$. For more hydrophilic surfaces, such as glass and acrylic, the We dependence is much weaker as shown in Fig. 9.

V. THEORETICAL ANALYSIS

The retracting droplet in the inertial mode presents a well-defined rim-lamella structure, which has been utilized in recent works [42,47,60,61] when modeling the droplet spreading and its maximum spread factor. In contrast, the droplet shape in the capillary mode can be very complicated due to the collapse of the rim and the propagation of capillary waves on the liquid-air interface. Therefore, the modeling of the retraction rate for the capillary mode will be left for future investigations. In the current study, we focus on modeling the inertial-mode retraction in order to correctly reveal the dependence of $\dot{\epsilon}_i$ on We.

Such dependence on We cannot be derived from the previous retraction theory [39]. By normalizing $\dot{\epsilon}_i$ with V_0/R_0, the original equation [Eq. (3.2) in Ref. [39]] can be written as

$$\left(\frac{\dot{\epsilon}_i}{V_0/R_0}\right)\mathrm{We}^{1/2} \sim \sqrt{\left(1 - \cos\theta_{r,s}\right)}. \tag{3}$$

In the classical theory, the static receding contact angle is used in Eq. (3), which is considered not dependent on We. Therefore, the classical theory indicates that for a given surface, the left-hand side term in Eq. (3) should remain unchanged. Figure 10 plots the measurement of this term at different We for the six surfaces. The dependence of this term on We can be clearly observed, which contradicts the classical theory.

The first thing one can question in Eq. (3) is the substitution of $\theta_{r,s}$. Under real conditions, it should be replaced with the dynamic receding contact angle ($\theta_{r,d}$), which is related to the instantaneous contact line retracting velocity [$V_{cl} = -\dot{R}(t)$]. This reshapes Eq. (3) into the following:

$$\left(\frac{\dot{\epsilon}_i}{V_0/R_0}\right)\mathrm{We}^{1/2} \sim \sqrt{\left(1 - \cos\theta_{r,d}\right)} \sim \sqrt{\{1 - \cos[f(V_{cl})]\}}. \tag{4}$$

Because the retraction rate is also related to the contact line velocity [$\dot{\epsilon}_i \sim \max(V_{cl})/R_{\max}$], a simple scaling cannot be obtained from Eq. (4). The current study aims at explaining the general variation of the retraction rate with respect to the impacting Weber number. Therefore, the
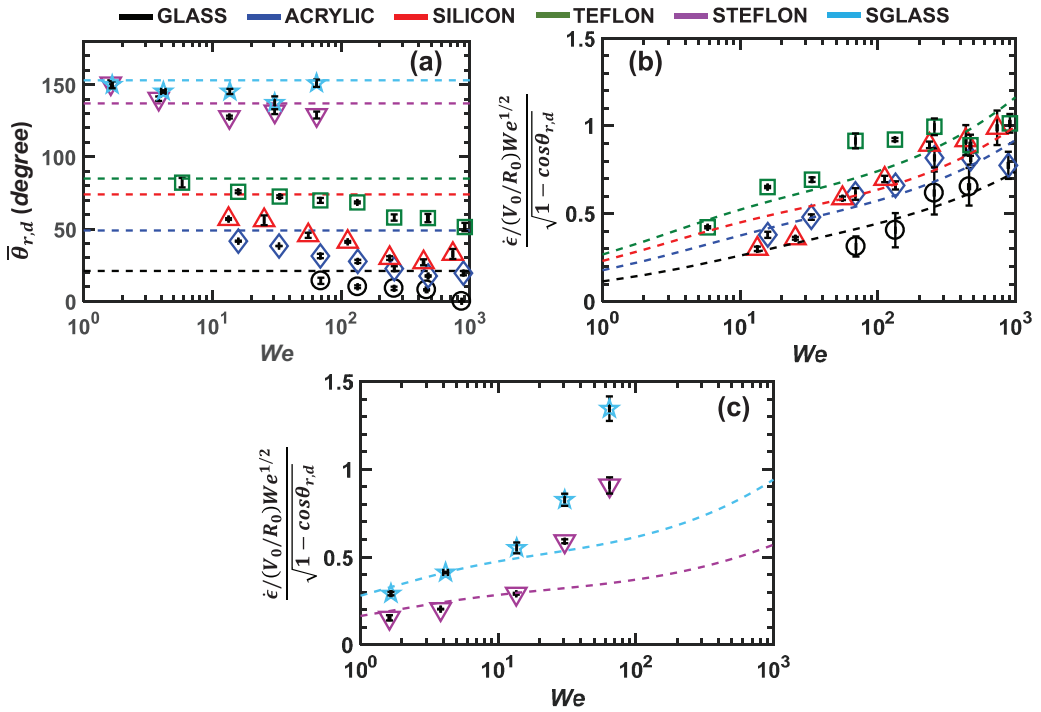
FIG. 11. (a) Averaged dynamic receding contact angles during the inertial-mode retraction process for different surfaces. The dashed lines indicate $\theta_{r,s}$ for corresponding surface. (b) The ratio of the left-hand side to the right-hand side of (3) after the substitution of $\theta_{r,d}$ for hydrophilic and hydrophobic surfaces; (c) The corresponding ratio for the two superhydrophobic surfaces. [The dashed lines in (b) and (c) are from Eq. (10).]

relatively small change of the receding contact angle (Fig. 7) during the inertial regime is neglected, and an averaged dynamic receding contact angle $\{\bar{\theta}_{r,d} = \mathrm{mean}[\theta_{r,d}(t = t_r \sim t_i)]\}$ is adopted for simplicity. Figure 11(a) shows the variation of the averaged dynamic receding contact angle during inertial-mode retraction at different We. In general, $\bar{\theta}_{r,d}$ appears to be smaller than $\bar{\theta}_{r,s}$ denoted by corresponding dashed lines. Moreover, the apparent $\bar{\theta}_{r,d}$ slightly decreases with the increase of We. Figures 11(b) and 11(c) plot the ratio of the left-hand-side to the right-hand-side term in Eq. (3) after the replacement of $\theta_{r,s}$ by $\bar{\theta}_{r,d}$ for hydrophilic/hydrophobic and superhydrophobic surfaces, respectively. This calculated ratio is dependent on We as shown from Figs. 11(b) and 11(c). The revealed increasing trend indicates that other important factors which depend upon We, other than $\bar{\theta}_{r,d}$, should be accounted for in order to explain the trend observed from the experiments.

Now, let us take a step back when deriving the classical theories. An intermediate equation describing the retraction of the surrounding rim reads [39]

$$h_l V_{\mathrm{ret}}^2 \sim f(\bar{\theta}_{r,d}) \sim 1 - \cos\bar{\theta}_{r,d}, \qquad (5)$$

where h_l is the lamella thickness, V_{ret} is droplet retraction velocity, and $f(\bar{\theta}_{r,d})$ denotes a function of the averaged dynamic receding contact angle. Equation (5) is given by Bartolo *et al.* [39] by considering the retracting droplet as an analogy to an inertial-dewetting thin film [40,41].

It should be noted that Eq. (5) can also be derived from the rim motion equation, which is specially developed for droplet spreading and receding on a solid surface [42,60,62], based on the following assumptions: (1) steady-state retraction process, (2) negligible viscous forces, and (3) negligible velocity field in the central film.
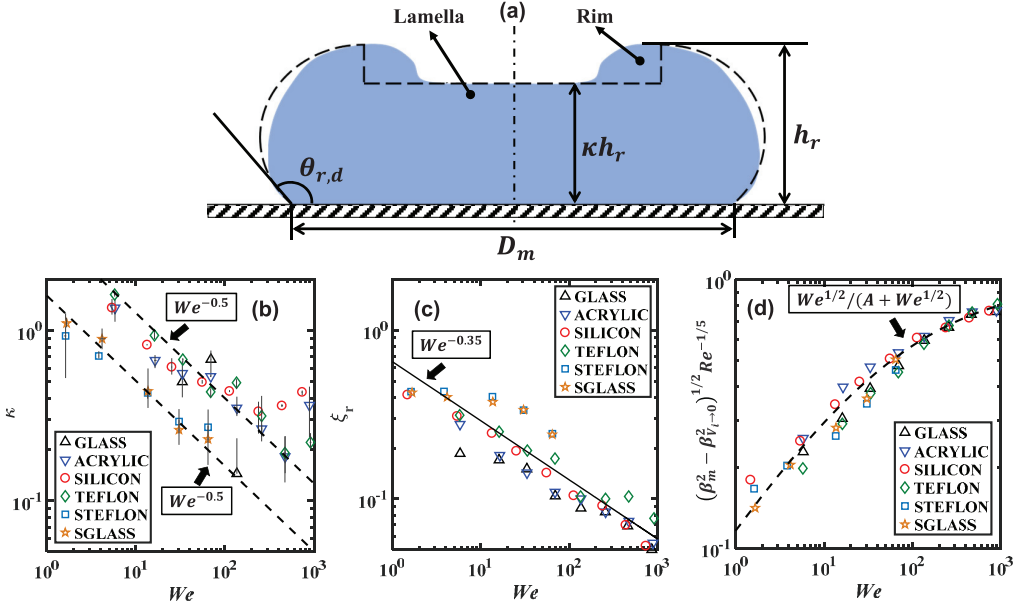
FIG. 12. (a) The shape assumption of retracting droplet and the variation of (b) shape factor κ, (c) dimensionless rim height ξ_r, and (d) maximum spread factor β_m with We.

These assumptions can be reasonably justified from the experimental retraction curves (Fig. 7), the low viscosity of the DI water, and the relatively long time after impact. Therefore, the retraction rate for the inertial mode can be derived from Eq. (5) as

$$\dot{\epsilon}_i = \frac{V_r}{R_m} \sim \sqrt{\frac{f(\bar{\theta}_{r,d})}{h_l R_m^2}}. \tag{6}$$

A rough estimation of h_l was used by Bartolo et al. [39], who treated the droplet shape as a cylindrical disk. This makes $h_l R_m^2$ to be a constant related only to the droplet initial volume. However, from previous investigations [47,63,64], it was shown that the impacting droplet better fits a rim-lamella shape rather than a cylindrical disk shape, which can also be justified here from the insets in Fig. 7. In order to account for the influence of the droplet shape assumption on the prediction of $\dot{\epsilon}_i$, a droplet shape proposed by Wang et al. [47] is utilized, which has been applied to model the maximum spread factor (β_m). A sketch of the shape assumption is presented in Fig. 12(a). The volume conservation when assuming the shape in Fig. 12(a) for the initial retracting droplet gives the following:

$$\left[\frac{1}{(1 - \cos \bar{\theta}_{r,d})^2} - \frac{1}{3} \frac{1 - \cos^3 \bar{\theta}_{r,d}}{(1 - \cos \bar{\theta}_{r,d})^3} \right] \xi_r^3 + \frac{(\bar{\theta}_{r,d} - 1/2 \sin 2\bar{\theta}_{r,d})}{(1 - \cos \bar{\theta}_{r,d})^2} \left(\frac{1}{2} \beta_m - \xi_r \frac{\sin \bar{\theta}_{r,d}}{1 - \cos \bar{\theta}_{r,d}} \right) \xi_r^2$$

$$+ \kappa \xi_r \left(\frac{1}{2} \beta_m - \xi_r \frac{\sin \bar{\theta}_{r,d}}{1 - \cos \bar{\theta}_{r,d}} \right)^2 = \frac{1}{6}. \tag{7}$$

κ in Eq. (7) is called the shape factor [47], which characterizes the ratio of the lamella thickness to the surrounding rim height (h_l/h_r). β_m is the maximum spread factor ($\beta_m = R_m/R_0$), and ξ_r is the dimensionless rim height ($\xi_r = h_r/2R_0$). A difference is that the averaged dynamic receding contact angle ($\bar{\theta}_{r,d}$) is used in Eq. (7) instead of the dynamic advancing contact angle ($\theta_{a,d}$). Because ξ_r, β_m, and $\theta_{r,d}$ are experimentally available, the values of κ can be then calculated from Eq. (7). The

variation of κ is demonstrated in Fig. 12(b) for a range of We from 10^0 to 10^3. The dashed curves in Fig. 12(b) denote the scaling relationship for κ with respect to We. It is shown that the scaling for all the six surfaces roughly remains the same as $We^{-0.5}$, although the absolute values of κ for the superhydrophobic surfaces are generally smaller. The variation of ξ_r measured from the experiment is demonstrated in Fig. 12(c). It is shown that the variation of ξ_r with We can also be estimated by a simple scaling as $\xi_r \sim We^{-0.35}$. Finally, a universal scaling as proposed in Ref. [65,66] is adopted for correlating β_m as

$$\left(\beta_m^2 - \beta_{V_i \to 0}^2\right)^{1/2} Re^{-1/5} = We^{1/2}/(A + We^{1/2}), \tag{8}$$

where A is a constant of 7.6, the same as what was suggested in Ref. [65]. $\beta_{V_i \to 0}$ is the droplet spreading factor at zero impact velocities. The details about the determination of $\beta_{V_i \to 0}$ are included in the Supplemental Material [59]. It is shown from Fig. 12(d) that the universal scaling in Eq. (8) can well correlate the experimental measurements of β_m. Because the current study deals only with water droplets, the viscous effects on the retraction rate will be neglected for simplicity, which may not be true for more viscous liquid droplets. Then the Reynolds number can be correlated by the Weber number as $Re = BWe^{1/2}$, where B is a constant of 450 for the current experiment. Therefore, the correlation of β_m, with respect to We only, becomes

$$\beta_m = \sqrt{\beta_{V_i \to 0}^2 + \left[\frac{We^{1/2}}{A + We^{1/2}}\right]^2 B^{2/5} We^{1/5}}. \tag{9}$$

Up to this point, the dependence of $\bar{\theta}_{r,d}$, κ, ξ_r, and β_m on We have been determined. After taking $f(\bar{\theta}_{r,d})$ on the right-hand side of Eq. (6) and normalizing $\dot{\epsilon}_i$ by V_0/R_0 as was done in Eq. (3), the following relationship can be obtained:

$$\frac{\left(\frac{\dot{\epsilon}_i}{V_0/R_0}\right) We^{\frac{1}{2}}}{\sqrt{1 - \cos\bar{\theta}_{r,d}}} \sim \sqrt{\frac{1}{h_l R_m^2}} \sim \sqrt{\frac{1}{\kappa \xi_r \beta_m^2}} \sim \sqrt{\frac{1}{We^{-0.5} We^{-0.35} \left\{\beta_{V_i \to 0}^2 + \left[\frac{We^{\frac{1}{2}}}{A + We^{\frac{1}{2}}}\right]^2 B^{\frac{2}{3}} We^{\frac{1}{5}}\right\}}}$$

$$\sim \sqrt{\frac{We^{0.85}}{\beta_{V_i \to 0}^2 + \left[\frac{We^{1/2}}{A + We^{1/2}}\right]^2 B^{2/5} We^{1/5}}}. \tag{10}$$

The scaling in Eq. (10) correlates well with the experimental data for hydrophilic and hydrophobic surfaces as demonstrated in Fig. 11(b) and reasonably reveal the increasing trend as observed in the experiment. For the two superhydrophobic surfaces, the predictions by Eq. (10) underestimate significantly for $We > 30$, which is explained below. The analysis above indicates that the increasing trend of $\dot{\epsilon}_i$ mainly results from the decrease of the lamella thickness with increasing We. The estimation of the lamella thickness during the retraction process can be obtained through examining the classical theories for droplet spreading on solid surfaces [60]. For the small capillary numbers ($0.002 \leqslant Ca = \mu V_0/D_0 \leqslant 0.06$) in the experiment, the approximate solutions for the droplet spreading and receding in the case $Re \gg We$ can be reasonably adopted. The dimensionless retraction starting time can then be calculated as [60]

$$\tau_r = \left[\frac{\eta_1 We \beta_m^2}{1 - \cos\bar{\theta}_{r,d}}\right]^{1/4} - \tau_1, \tag{11}$$

where τ_1 and η_1 are constants determined by certain initial conditions [60,67]. In the current analysis, the film thickness during the retraction process will be assumed to be large compared to the boundary layer thickness. Therefore, the asymptotic solution for the film thickness in the
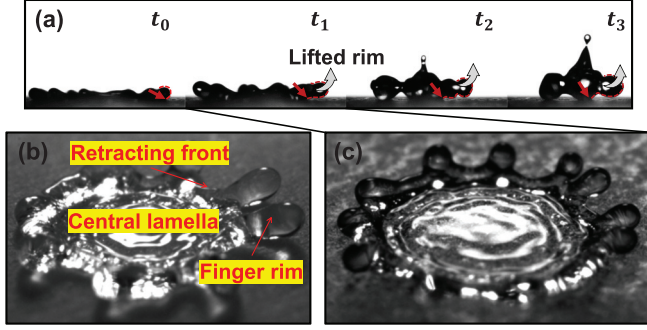
FIG. 13. (a) Image sequences showing droplet retraction at relatively large We on Sglass; (b) fingering pattern for droplet retracting on STeflon; (c) fingering pattern for droplet retracting on Sglass.

inviscid region is adopted here as follows [60]:

$$\xi_l = \frac{\eta_1}{(\tau + \tau_1)^2}. \tag{12}$$

By substituting Eq. (11) into Eq. (12), the dimensionless film thickness during the inertial-mode retraction process can be obtained as

$$\xi_{l,r} = \sqrt{\frac{\eta_1(1 - \cos\bar{\theta}_{r,d})}{\mathrm{We}\beta_m^2}} \sim \sqrt{\frac{1}{\mathrm{We}\beta_m^2}}. \tag{13}$$

Therefore, the following can be obtained based on the spreading theory from Roisman *et al.* [60]:

$$\frac{\left(\frac{\dot{\epsilon}_i}{V_0/R_0}\right)\mathrm{We}^{\frac{1}{2}}}{\sqrt{1 - \cos\bar{\theta}_{r,d}}} \sim \sqrt{\frac{1}{\xi_{l,r}\beta_m^2}} \sim \sqrt{\frac{1}{\sqrt{1/(\mathrm{We}\beta_m^2)}\beta_m^2}} \sim \sqrt{\frac{\mathrm{We}^{0.5}}{\sqrt{\beta_{V_i\to 0}^2 + \left[\frac{\mathrm{We}^{1/2}}{A+\mathrm{We}^{1/2}}\right]^2 B^{2/5}\mathrm{We}^{1/5}}}}. \tag{14}$$

The scaling correlation in Eq. (14) predicts a weaker increasing trend than Eq. (10), as compared in the Supplemental Material [59]. Moreover, it is shown that both Eq. (10) and Eq. (14) underestimate the increase for the two superhydrophobic surfaces when We > 30. This is believed to be caused by the air entrapment beneath the retracting droplet on the superhydrophobic surfaces. From the experimental videos, the abrupt increase when We > 30 corresponds to the occurrence of the fingering instability during the retraction on the superhydrophobic surfaces. Figure 13(a) demonstrates the sequence of droplet retraction on the Sglass surface. It is shown that from the time instance at t_1, the surrounding rim becomes finger-shaped as demonstrated in Figs. 13(b) and 13(c) for droplet retracting at We = 64 on STeflon and Sglass surfaces, respectively. The rim fingers keep being lifted up during the retraction process, and the retracting front between the fingers quickly moves back toward the center. In this case, the structure of the retracting droplets may differ significantly from the assumed shape for the inertial-mode retraction. A further investigation of the retraction rate for droplet retraction of such a mode deserves future efforts, which can account for both the influence of the droplet structure and the instabilities during the retraction process.

VI. SCALING OF THE RETRACTION CURVES

The last discussion is about the scaling of the retraction curves. As aforementioned in the introduction, a universal normalized retraction curve ($[D(t)/D_{\max}]$ vs $[t]$) for different We is questionable. We start from analyzing the experimental data and then propose a normalization of the retraction curves.
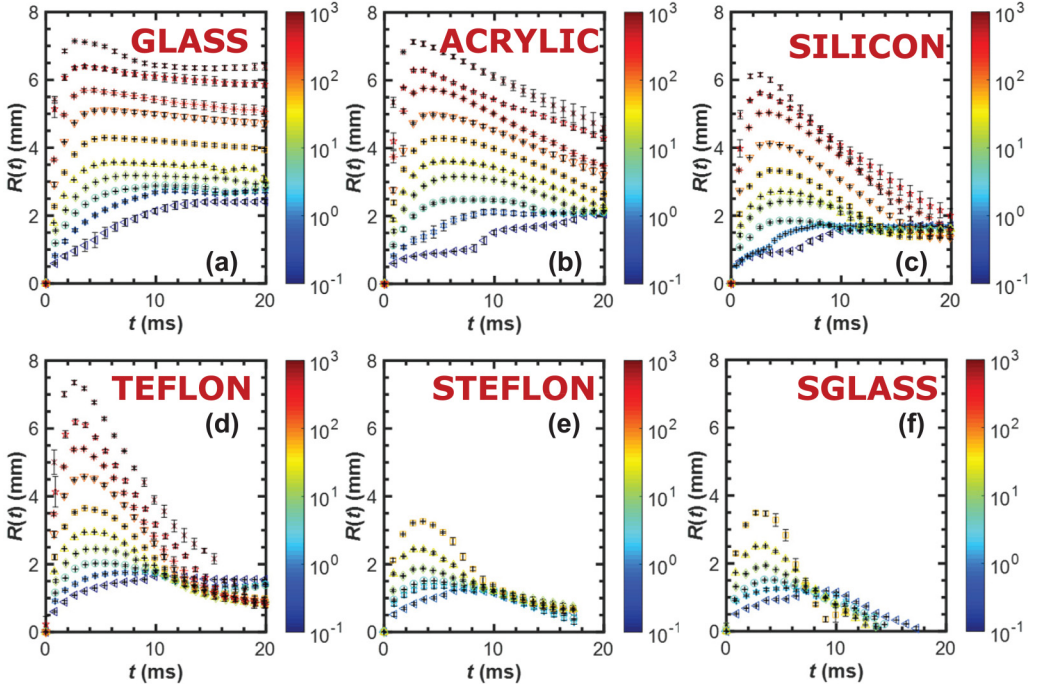
FIG. 14. Temporal evolution of $R(t)$ on (a) glass, (b) acrylic, (c) silicon, (d) Teflon, (e) STeflon, and (f) Sglass surfaces for different We indicated by the color bar. Error bars are included in the plots.

Figures 14(a)–14(f) plot the temporal evolution of the droplet spreading radius. Error bars in these plots are calculated from three repetitions. Only data points at selected time instances are plotted for clarity. It is shown that the error bars are much smaller than the difference between the two adjacent curves caused by the change in We. This indicates that the failure of the collapse of retraction curves should not be attributed to the measurement errors, but indeed to the variation in We. Relatively high measurement errors can be observed for some cases with very high We on acrylic and Teflon. They both result from the random satellite droplets left behind the retracting TPCL on the surfaces. From these dimensional retraction curves, one can observe that the average droplet retraction speed generally increases with the increase of $\theta_{r,s}$, which can be seen from the increase of the slopes. When the hydrophobicity increases, the dimensional retraction curves get closer to each other as shown in Figs. 14(d)–14(f). From Fig. 14, it is found that the TPCL does not retract immediately after it reaches its maximum spreading, verifying the existence of the contact angle relaxation phase [38] between the spreading and retraction processes, as defined in Fig. 7. Figures 15(a)–15(f) show the variations of t_s and t_r with different We. Both t_s and t_r decrease with increasing We, which is consistent with Antonini et $al.$'s findings [38]. The shaded area in Fig. 15 denotes the contact angle relaxation period Δt_{β_m}. With increasing We, the gap becomes narrower, meaning that Δt_{β_m} is getting smaller. Moreover, it is shown that the surface hydrophobicity tends to decrease Δt_{β_m}.

From the above discussion, it is seen that one of the reasons accounting for the failure of collapse of the normalized retraction curves comes from the difference in t_r. Therefore, it is more reasonable to put all the retraction curves for different We onto a universal starting point (t_r, R_m). Additionally, we further make the retraction curves terminate at the end of the capillary retraction process (t_c, R_c), which has been defined in Fig. 7. The normalized abscissa and ordinate are $[R(t) - R_c]/(R_m - R_c)$ and $(t - t_r)/(t_c - t_r)$, respectively. Such a scaling of the retraction curves is demonstrated in Fig. 16. It is shown that compared to the normalization by R_m in the Supplemental
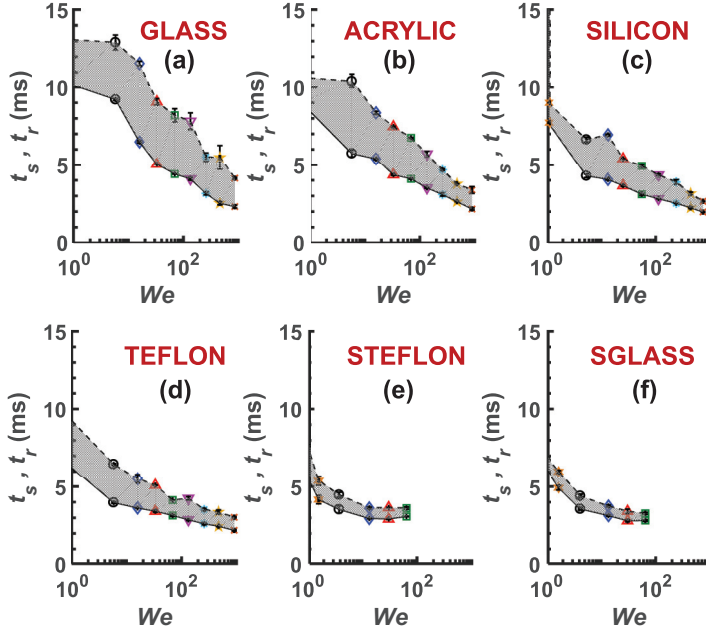
FIG. 15. The spreading time and retraction start time at different We.

Material [59] based on previous publications, the proposed normalization in Fig. 16 can actually reveal certain similarity features of the droplet retraction process in the inertial-capillary regime: normalized retraction curves at different impact conditions generally collapse into a universal curve. For the glass surface and very low We on other surfaces, certain deviations exist from the universal curve. This may be attributed to the relatively weak retraction motions for such conditions. As mentioned earlier, the wetting state for a droplet impacting onto the Sglass surface always stays at the Cassie-Baxter state. However, for the STeflon surface, the retracting droplet experiences a Cassie-to-Wenzel transition when We changes. From Fig. 16(e), it is shown that the universal curve for these two different wetting states can be different. Last but not the least, this proposed scaling can also give us a physical interpretation for the derivative of the normalized retraction curves. The derivative of the normalized retraction curves, $V_{ret}/[(R_m - R_c)/(t_c - t_r)]$, represents the ratio of

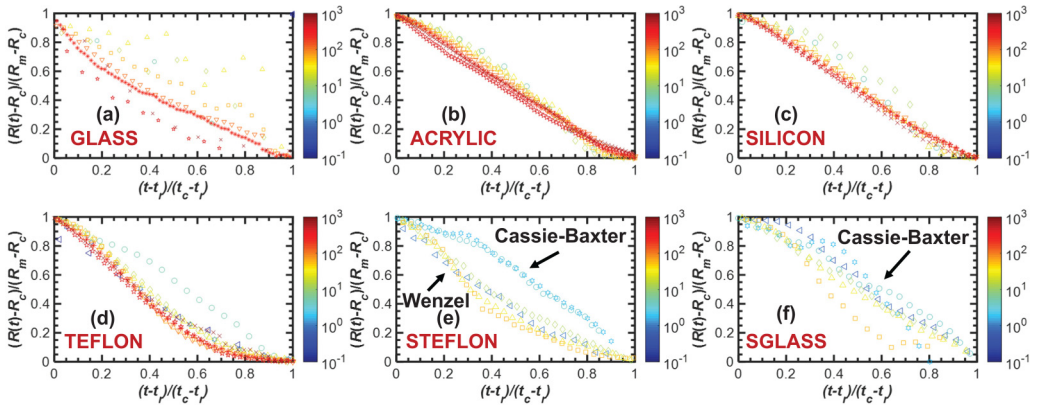

FIG. 16. Newly normalized retraction curves for the six surfaces.

the instantaneous retraction velocity (V_{ret}) to the average retraction velocity of the whole retraction process [$\bar{V}_{\text{ret}} = (R_m - R_c)/(t_c - t_r)$].

VII. CONCLUSIONS

A comprehensive study of water droplet retraction dynamics was carried out on six solid surfaces with varying wettabilities at different We. The morphologies of retracting droplets have been summarized and compared. Three distinct retraction modes are classified based on the retracting morphologies: inertial mode, capillary mode, and spherical-cap mode.

Specifically, a detailed characterization is presented for the inertial and capillary modes. The inertial mode occupies the early stage of the retraction process, while the capillary mode dominates the later one. During the inertial-mode retraction, the retracting droplet features a rim-lamella structure with a slowly decreasing dynamic receding contact angle ($\theta_{r,d}$). However, during the capillary-mode retraction, $\theta_{r,d}$ varies with the propagation of the capillary waves released from the collapse of the rim and lamella towards the three-phase contact line (TPCL). A comparison of the occupied periods reveals that at small We, the capillary mode occupies most of the retraction process. With higher We, the inertial mode starts to dominate the retraction process for more hydrophilic surfaces. However, for hydrophobic and superhydrophobic surfaces, the capillary mode is always the primary mode for droplet retraction.

The dependency of the retraction rate ($\dot{\epsilon}$) on Weber number and surface wettabilities was investigated experimentally and theoretically. Experimental measurements demonstrate that $\dot{\epsilon}_i$ generally increases with increasing We, while for the capillary mode, $\dot{\epsilon}_c$ tends to decrease. At high We, $\dot{\epsilon}$ reaches an asymptotic value independent of We. This indicates that for high-We droplet retraction, the retraction rate is a material constant only. The influence of the surface wettability is clear: both $\dot{\epsilon}_i$ and $\dot{\epsilon}_c$ are higher for the more hydrophobic surface with a higher static receding contact angle ($\theta_{r,s}$). Moreover, it is shown that the dependency of $\dot{\epsilon}$ on We tends to be stronger for more hydrophobic surfaces. Particularly, a semiempirical model is proposed to explain the We dependency of the retraction rate for the inertial mode ($\dot{\epsilon}_i$). In the proposed model, the retracting droplet adopts a rim-lamella structure considering a We-dependent averaged dynamic receding contact angle ($\bar{\theta}_{r,d}$) and a shape factor ($\kappa = h_l/h_r$). The model gives a scaling as [$\dot{\epsilon}_i/(V_0/R_0)$]We$^{1/2}/\sqrt{1 - \cos\bar{\theta}_{r,d}} \sim \sqrt{\text{We}^{0.85}/\{\beta_{V_i \to 0}^2 + [\frac{\text{We}^{1/2}}{A + \text{We}^{1/2}}]^2 B^{2/5}\text{We}^{1/5}\}}$, which can well explain the dependence of $\dot{\epsilon}_i$ on impacting We. A similar scaling [$\sim\sqrt{\text{We}^{0.5}/\sqrt{\beta_{V_i \to 0}^2 + (\frac{\text{We}^{1/2}}{A + \text{We}^{1/2}})^2 B^{2/5}\text{We}^{1/5}}}$] can also be derived from the asymptotic solution for inviscid droplets impacting on solid surfaces, which also predicts the increase of $\dot{\epsilon}_i$ with increasing We. The influence of the dynamic receding contact angle on the retraction rate is neglected in the proposed model, which needs further scrutiny for a more accurate correlation for the retraction rate.

Finally, a scaling of the retraction curves is proposed to reveal similarity behavior during the droplet retraction process. The classically normalized retraction curves ([$R(t)/R_m$] vs [t]) fail to collapse into a universal curve for DI-water droplet retractions due to low viscosity. Moreover, the contact angle relaxation phase can cause the shift of the normalized retraction curves at different We. The retraction curves normalized in the way we propose ($\{[R(t) - R_c]/(R_m - R_c)\}$ vs [$(t - t_r)/(t_c - t_r)$]) are found to collapse well into each other. The derivative of these normalized curves can be physically interpreted as the ratio of the instantaneous retraction velocity to the mean retraction velocity.

ACKNOWLEDGMENTS

[1] C. Antonini, I. Bernagozzi, S. Jung, D. Poulikakos, and M. Marengo, Water Drops Dancing on Ice: How Sublimation Leads to Drop Rebound, Phys. Rev. Lett. **111**, 014501 (2013).

[2] J. C. Bird, R. Dhiman, H. M. Kwon, and K. K. Varanasi, Reducing the contact time of a bouncing drop, Nature (London) **503**, 385 (2013).

[3] Y. Liu, G. Whyman, E. Bormashenko, C. Hao, and Z. Wang, Controlling drop bouncing using surfaces with gradient features, Appl. Phys. Lett. **107**, 051604 (2015).

[4] T. M. Schutzius, S. Jung, T. Maitra, G. Graeber, M. Köhme, and D. Poulikakos, Spontaneous droplet trampolining on rigid superhydrophobic surfaces, Nature (London) **527**, 82 (2015).

[5] C. Antonini, S. Jung, A. Wetzel, E. Heer, P. Schoch, A. M. Moqaddam, S. S. Chikatamarla, I. Karlin, M. Marengo, and D. Poulikakos, Contactless prompt tumbling rebound of drops from a sublimating slope, Phys. Rev. Fluids **1**, 013903 (2016).

[6] C. Lv, P. Hao, X. Zhang, and F. He, Drop impact upon superhydrophobic surfaces with regular and hierarchical roughness, App. Phys. Lett. **108**, 141602 (2016).

[7] T. Vasileiou, J. Gerber, J. Prautzsch, T. M. Schutzius, and D. Poulikakos, Superhydrophobicity enhancement through substrate flexibility, Proc. Natl. Acad. Sci. USA **113**, 13307 (2016).

[8] S. Yun, Controlling the residence time of a bouncing drop with asymmetric shaping, Soft Matter **14**, 4946 (2018).

[9] T. Gao, J. Li, Y. Liu, and J. Luo, Self-retraction of surfactant droplets on a superhydrophilic surface, Langmuir **34**, 15388 (2018).

[10] A. M. Moqaddam, S. S. Chikatamarla, and I. V. Karlin, Drops bouncing off macro-textured superhydrophobic surfaces, J. Fluid Mech. **824**, 866 (2017).

[11] V. Bergeron, D. Bonn, J. Y. Martin, and L. Vovelle, Controlling droplet deposition with polymer additives, Nature (London) **405**, 772 (2000).

[12] D. Bartolo, A. Boudaoud, G. Narcy, and D. Bonn, Dynamics of Non-Newtonian Droplets, Phys. Rev. Lett. **99**, 174502 (2007).

[13] M. Aytouna, D. Bartolo, G. Wegdam, D. Bonn, and S. Rafaï, Impact dynamics of surfactant laden drops: Dynamic surface tension effects, Exp. Fluids **48**, 49 (2010).

[14] D. Zang, X. Wang, X. Geng, Y. Zhang, and Y. Chen, Impact dynamics of droplets with silica nanoparticles and polymer additives, Soft Matter **9**, 394 (2013).

[15] A. Alizadeh, V. Bahadur, W. Shang, Y. Zhu, D. Buckley, A. Dhinojwala, and M. Sohal, Influence of substrate elasticity on droplet impact dynamics, Langmuir **29**, 4520 (2013).

[16] S. Yun and G. Lim, Ellipsoidal drop impact on a solid surface for rebound suppression, J. Fluid Mech. **752**, 266 (2014).

[17] M. Damak, S. R. Mahmoudi, M. N. Hyder, and K. K. Varanasi, Enhancing droplet deposition through in-situ precipitation, Nat. Commun. **7**, 12560 (2016).

[18] K. A. Raman, R. K. Jaiman, Y. Sui, T. S. Lee, and H. T. Low, Rebound suppression of a droplet impacting on an oscillating horizontal surface, Phys. Rev. E **94**, 023108 (2016).

[19] M. Song, J. Ju, S. Luo, Y. Han, Z. Dong, Y. Wang, Z. Gu, L. Zhang, R. Hao, and L. Jiang, Controlling liquid splash on superhydrophobic surfaces by a vesicle surfactant, Sci. Adv. **3**, e1602188 (2017).

[20] G. J. Dorr, S. Wang, L. C. Mayo, S. W. Mccue, W. A. Forster, J. Hanan, and X. He, Impaction of spray droplets on leaves: influence of formulation and leaf character on shatter, bounce and adhesion, Exp. Fluids **56**, 143 (2015).

[21] Y. Xu, S. Vincent, Q. C. He, and H. Le-quang, Spread and recoil of liquid droplets impacting on solid surfaces with various wetting properties, Surf. Coat. Technol. **357**, 140 (2019).

[22] B. Lojewski, W. Yang, H. Duan, C. Xu, and W. Deng, Design, fabrication, and characterization of linear multiplexed electrospray atomizers micro-machined from metal and polymers, Aerosol Sci. Technol. **47**, 146 (2013).

[23] X. Deng, L. Mammen, Y. Zhao, P. Lellig, K. Müllen, C. Li, H. J. Butt, and D. Vollmer, Transparent, thermally stable and mechanically robust superhydrophobic surfaces made from porous silica capsules, Adv. Mater. **23**, 2962 (2011).

[24] T. M. Schutzius, S. Jung, T. Maitra, P. Eberle, C. Antonini, C. Stamatopoulos, and D. Poulikakos, Physics of icing and rational design of surfaces with extraordinary icephobicity, Langmuir **31**, 4807 (2014).

[25] M. I. Smith and J. S. Sharp, Origin of contact line forces during the retraction of dilute polymer solution drops, Langmuir **30**, 5455 (2014).

[26] X. Li, X. Ma, and Z. Lan, Behavioral patterns of drop impingement onto rigid substrates with a wide range of wettability and different surface temperatures, AIChE J. **55**, 1983 (2009).

[27] J. H. Moon, D. Y. Kim, and S. H. Lee, Spreading and receding characteristics of a non-Newtonian droplet impinging on a heated surface, Exp. Therm. Fluid Sci. **57**, 94 (2014).

[28] S. Sen, V. Vaikuntanathan, and D. Sivakumar, Impact dynamics of alternative jet fuel drops on heated stainless steel surface, Int. J. Therm. Sci. **121**, 99 (2017).

[29] X. Li, X. Ma, and Z. Lan, Dynamic behavior of the water droplet impact on a textured hydrophobic/superhydrophobic surface: The effect of the remaining liquid film arising on the pillars' tops on the contact time, Langmuir **26**, 4831 (2010).

[30] P. B. Weisensee, J. Ma, Y. H. Shin, J. Tian, Y. Chang, W. P. King, and N. Miljkovic, Droplet impact on vibrating superhydrophobic surfaces, Phys. Rev. Fluids **2**, 103601 (2017).

[31] J. B. Lee, S. Dos Santos, and C. Antonini, Water touch-and-bounce from a soft viscoelastic substrate: Wetting, dewetting, and rebound on bitumen, Langmuir **32**, 8245 (2016).

[32] P. B. Weisensee, J. Tian, N. Miljkovic, and W. P. King, Water droplet impact on elastic superhydrophobic surfaces, Sci. Rep. **6**, 30328 (2016).

[33] Y. H. Yeong, J. Burton, E. Loth, and I. S. Bayer, Drop impact and rebound dynamics on an inclined superhydrophobic surface, Langmuir **30**, 12027 (2014).

[34] C. Antonini, F. Villa, and M. Marengo, Oblique impacts of water drops onto hydrophobic and superhydrophobic surfaces: Outcomes, timing, and rebound maps, Exp. Fluids **55**, 1713 (2014).

[35] D. Richard, C. Clanet, and D. Quéré, Surface phenomena: Contact time of a bouncing drop, Nature (London) **417**, 811 (2002).

[36] K. Okumura, F. Chevy, D. Richard, D. Quéré, and C. Clanet, Water spring: A model for bouncing drops, Eur. Phys. Lett. **62**, 237 (2003).

[37] L. Rayleigh, On the capillary phenomena of jets, Proc. R. Soc. Lond. **29**, 71 (1879).

[38] C. Antonini, A. Amirfazli, and M. Marengo, Drop impact and wettability: From hydrophilic to superhydrophobic surfaces, Phys. Fluids **24**, 102104 (2012).

[39] D. Bartolo, C. Josserand, and D. Bonn, Retraction dynamics of aqueous drops upon impact on non-wetting surfaces, J. Fluid Mech. **545**, 329 (2005).

[40] G. I. Taylor, The dynamics of thin sheets of fluid. III. Disintegration of fluid sheets, Proc. R. Soc. Lond. A **253**, 313 (1959).

[41] F. E. C. Culick, Comments on a ruptured soap film, J. Appl. Phys. **31**, 1128 (1960).

[42] J. Eggers, M. A. Fontelos, C. Josserand, and S. Zaleski, Drop dynamics after impact on a solid wall: Theory and simulations, Phys. Fluids **22**, 062101 (2010).

[43] Y. Zhu, H. R. Liu, K. Mu, P. Gao, H. Ding, and X. Y. Lu, Dynamics of drop impact onto a solid sphere: Spreading and retraction, J. Fluid Mech. **824**, R3 (2017).

[44] M. Damak and K. Varanasi, Expansion and retraction dynamics in drop-on-drop impacts on nonwetting surfaces, Phys. Rev. Fluids **3**, 093602 (2018).

[45] T. Bobinski, G. Sobieraj, M. Psarski, G. Celichowski, and J. Rokicki, Droplet bouncing on the surface with micro-structure, Arch. Mech. **69**, 177 (2017).

[46] S. Lin, B. Zhao, S. Zou, J. Guo, Z. Wei, and L. Chen, Impact of viscous droplets on different wettable surfaces: Impact phenomena, the maximum spreading factor, spreading time and post-impact oscillation, J. Colloid Interface Sci. **516**, 86 (2018).

[47] F. Wang, L. Yang, L. Wang, Y. Zhu, and T. Fang, Maximum spread of droplet impacting onto solid surfaces with different wettabilities: Adopting a rim-lamella shape, Langmuir **35**, 3204 (2019).

[48] M. A. Nilsson, R. J. Daniello, and J. P. Rothstein, A novel and inexpensive technique for creating superhydrophobic surfaces using Teflon and sandpaper, J. Phys. D **43**, 045301 (2010).

[49] R. Gupta, V. Vaikuntanathan, and D. Sivakumar, Superhydrophobic qualities of an aluminum surface coated with hydrophobic solution NeverWet, Colloids Surf. A **500**, 45 (2016).

[50] C. Antonini, F. Villa, I. Bernagozzi, A. Amirfazli, and M. Marengo, Drop rebound after impact: The role of the receding contact angle, Langmuir **29**, 16045 (2013).

[51] A. B. D. Cassie and S. Baxter, Wettability of porous surfaces, Trans. Faraday Soc. **40**, 546 (1944).

[52] R. N. Wenzel, Resistance of solid surfaces to wetting by water, Ind. Eng. Chem. **28**, 988 (1936).

[53] F. Wang and T. Fang, Post-impact drop vibration on a hydrophilic surface, Exp. Therm. Fluid Sci. **98**, 420 (2018).

[54] D. Khojasteh, M. Kazerooni, S. Salarian, and R. Kamali, Droplet impact on superhydrophobic surfaces: A review of recent developments, J. Ind. Eng. Chem. **42**, 1 (2016).

[55] E. S. Quintero, G. Riboux, and J. M. Gordillo, Splashing of droplets impacting superhydrophobic substrates, J. Fluid Mech. **870**, 175 (2019).

[56] D. Bartolo, F. Bouamrirene, E. Verneuil, A. Buguin, P. Silberzan, and S. Moulinet, Bouncing or sticky droplets: Impalement transitions on superhydrophobic micropatterned surfaces, Euro. Phys. Lett. **74**, 299 (2006).

[57] A. M. Edwards, R. Ledesma-aguilar, M. I. Newton, C. V. Brown, and G. Mchale, Not spreading in reverse: The dewetting of a liquid film into a single drop, Sci. Adv. **2**, e1600183 (2016).

[58] T. C. de Goede, K. G. de Bruin, N. Shahidzadeh, and D. Bonn, Predicting the maximum spreading of a liquid drop impacting on a solid surface: Effect of surface tension and entrapped air layer, Phys. Rev. Fluids **4**, 053602 (2019).

[59] See Supplemental Material at http://link.aps.org/supplemental/10.1103/PhysRevFluids.5.033604 for determination of the zero-velocity spread factor, comparison of retraction rate predictions, and retraction curves normalized in traditional way.

[60] I. V. Roisman, R. Rioboo, and C. Tropea, Normal impact of a liquid drop on a dry surface: Model for spreading and receding, Proc. R. Soc. Lond. A **458**, 1411 (2002).

[61] P. Attané, F. Girard, and V. Morin, An energy balance approach of the dynamics of drop impact on a solid surface, Phys. Fluids **19**, 012101 (2007).

[62] J. M. Gordillo, G. Riboux, and E. S. Quintero, A theory on the spreading of impacting droplets, J. Fluid Mech. **866**, 298 (2019).

[63] G. Lagubeau, M. A. Fontelos, C. Josserand, A. Maurel, V. Pagneux, and P. Petitjeans, Spreading dynamics of drop impacts, J. Fluid Mech. **713**, 50 (2012).

[64] S. Wildeman, C. W. Visser, C. Sun, and D. Lohse, On the spreading of impacting drops, J. Fluid Mech. **805**, 636 (2016).

[65] J. B. Lee, N. Laan, K. G. de Bruin, G. Skantzaris, N. Shahidzadeh, D. Derome, J. Carmeliet, and D. Bonn, Universal rescaling of drop impact on smooth and rough surfaces, J. Fluid Mech. **786**, R4 (2016).

[66] N. Laan, K. G. de Bruin, D. Bartolo, C. Josserand, and D. Bonn, Maximum Diameter of Impacting Liquid Droplets, Phys. Rev. Appl. **2**, 044018 (2014).

[67] I. V. Roisman, E. Berberović, and C. Tropea, Inertia dominated drop collisions. I. On the universal flow in the lamella, Phys. Fluids **21**, 052103 (2009).